tvst

Article

Prediction of Retinal Ganglion Cell Counts Considering Various Displacement Methods From OCT-Derived Ganglion Cell–Inner Plexiform Layer Thickness

Janelle Tong[1,2], Jack Phu[1,2], David Alonso-Caneiro[3], Sieu K. Khuu[2], and Michael Kalloniatis[1,2]

[1] Centre for Eye Health, University of New South Wales (UNSW), Sydney, NSW Australia
[2] School of Optometry and Vision Science, University of New South Wales, Sydney, NSW Australia
[3] Queensland University of Technology, Contact Lens and Visual Optics Laboratory, Centre for Vision and Eye Research, School of Optometry and Vision Science, QLD, Australia

Correspondence: Michael Kalloniatis, School of Optometry and Vision Science, University of New South Wales, Sydney, NSW 2052, Australia.
e-mail: m.kalloniatis@unsw.edu.au

Received: November 28, 2021
Accepted: April 25, 2022
Published: May 16, 2022

Keywords: retinal ganglion cell; optical coherence tomography; displacement

Citation: Tong J, Phu J, Alonso-Caneiro D, Khuu SK, Kalloniatis M. Prediction of retinal ganglion cell counts considering various displacement methods from OCT-derived ganglion cell–inner plexiform layer thickness. Transl Vis Sci Technol. 2022;11(5):13, https://doi.org/10.1167/tvst.11.5.13

Purpose: To compare various displacement models using midget retinal ganglion cell to cone (mRGC:C) ratios and to determine viability of estimating RGC counts from optical coherence tomography (OCT)–derived ganglion cell–inner plexiform layer (GCIPL) measurements.

Methods: Four Drasdo model variations were applied to macular visual field (VF) stimulus locations: (1) using meridian-specific Henle fiber length along the stimulus circumference; (2) using meridian-specific differences in RGC receptive field and counts along the stimulus circumference; (3) per method (2), averaged across principal meridians; and (4) per method (3), with the stimulus center displaced only. The Sjöstrand model was applied (5) along the stimulus circumference and (6) to the stimulus center only. Eccentricity-dependent mRGC:C ratios were computed over displaced areas, with comparisons to previous models using sum of squares of the residuals (SSR) and root mean square error (RMSE). RGC counts estimated from OCT-derived ganglion cell layer (GCL) and GCIPL measurements, from 143 healthy participants, were compared using Bland–Altman analyses.

Results: Methods 1, 2, and 5 produced mRGC:C ratios most consistent with previous models (SSR 3.82, 4.07, and 3.02; RMSE 0.22, 0.23, and 0.20), while central mRGC:C ratios were overestimated by method 3 and underestimated by methods 4 and 6. RGC counts predicted from GCIPL measurements were within 16% of GCL-based counts, with no notable bias with increasing RGC counts.

Conclusions: Sjöstrand displacement and meridian-specific Drasdo displacement applied to VF stimulus circumferences produce mRGC:C ratios consistent with previous models. RGC counts can be estimated from OCT-derived GCIPL measurements.

Translational Relevance: Implementing appropriate displacement methods and deriving RGC estimates from relevant OCT parameters enables calculation of the number of RGCs responding to VF stimuli from commercial instrumentation.

Introduction

A fundamental concept underpinning vision is that a quantifiable relationship should exist between measures of visual function and the anatomic or physiologic processes responsible for this output.[1,2] Modern investigations of this often-called structure–function relationship commonly focus on comparison of retinal and visual field (VF) data, with variables including but not limited to utilized structural parameters, VF stimulus characteristics, retinal locations, and sampled cohorts influencing the resultant models.[3–5] Further knowledge of the intricacies involved in the

structure–function relationship is fundamental in improving understanding of the various clinical presentations of ocular pathologies, including glaucoma, and has promising applications in the optimization of technologies to improve detection of such pathologies in clinical settings.

Seminal models of the structure–function relationship have used ex vivo histologic retinal ganglion cell (RGC) measurements as the structural measure, with such models describing a generally linear relationship between RGC count and VF sensitivity within the central 15°.[6–8] However, for clinical applications, surrogate measurements of cell anatomy, such as retinal thickness measurements from optical coherence tomography (OCT), are required. While RGC counts have been estimated from ganglion cell layer (GCL) thickness measurements derived from OCT,[9–11] the GCL is often difficult to delineate due to similar reflectivity with the underlying inner plexiform layer (IPL), and in lieu of only sampling the GCL, inner retinal complexes such as the ganglion cell–inner plexiform layer (GCIPL) and the ganglion cell complex are commonly utilized in commercially available OCT instruments. Estimates of RGC counts from these complexes have not been quantified, which would be valuable for the application of findings of cellular structure–function models across a broader range of settings and instrumentations.

Furthermore, clinical investigations of the macular structure–function relationship are complicated by the lateral displacement of RGCs relative to their connecting photoreceptors secondary to Henle fibers,[12] meaning that the RGCs responding to VF stimuli are not located where these stimuli project onto the retina. Drasdo et al.[12] reported anatomic displacement of RGCs as well as models of RGC displacement based on cumulative receptive field densities, and these have subsequently been widely applied to adjust for displacement. However, the exact implementation of these models is variable, with mean displacement across all meridians,[10,13–15] meridian-specific displacements,[11,16] and meridian-specific anatomic displacement[17] having been applied across different studies. Moreover, while displacement of VF stimulus centers has been utilized previously, Montesano et al.[11] demonstrated that this method underestimates RGC counts parafoveally, and displacement at the VF stimulus circumference produces estimates closer to expected RGC receptive field counts. Sjöstrand et al.,[18] on the other hand, described RGC displacement based on Henle fiber and bipolar cell configuration and the subsequent model demonstrating a smaller maximum displacement at the parafovea with no differences between meridians observed. To aid choice of the most appropriate method to apply in structure–function analyses, it would be useful to verify whether these displacement methods and their various implementations substantially differ.

The aims of this study were twofold. First, it sought to compare various implementations of the Drasdo and Sjöstrand models by computing midget RGC to cone ratios (mRGC:C), with previously reported ratios used as an anatomic "ground-truth" framework.[19,20] mRGC:C ratios provide a logical anatomic framework with which to compare calculated mRGC numbers, with this ratio reported as at least 2:1 at the foveal center, corresponding to connections of one ON and one OFF mRGC to each cone centrally, and with progressive decrease with increasing eccentricity due to pooling of cone synapses onto cone bipolar cells; these calculations have been previously used to verify findings between histologic studies.[12,18,20] Second, RGC count estimates derived from GCIPL and GCL measurements were compared to determine the viability of predicting RGC numbers from clinically available data. These investigations aim to facilitate translation of classic studies of the structure–function relationship to clinical settings.

Methods

Histologic Data

Human RGC data were obtained from Curcio and Allen,[21] who reported mean RGC density (D_{RGC}) in cells per square millimeter along each principal meridian for six healthy retinas. Similar to previous studies,[6,9] D_{RGC} between meridians were determined using polar interpolation, assuming linear change in density, to generate a D_{RGC} map at a resolution of 0.005 mm per pixel. RGC counts (C_{RGC}) were then calculated by multiplying pixel-wise D_{RGC} by the area encompassed by each pixel. Cone density and count maps were generated using an identical procedure, using meridional cone densities for eight healthy retinas as reported by Curcio et al.[22]

Subsequently, midget RGC count (C_{mRGC}) maps were derived from eccentricity-dependent estimates of the proportion of midget RGCs (mRGCs) relative to total RGCs (tRGCs)[12,19]:

$$\text{mRGC} = 0.8928 \times \left(1 + \frac{r}{41.03}\right)^{-1} \times \text{tRGC}$$

where r is eccentricity in degrees. For this equation, the degree to millimeter conversion derived by Montesano et al.[11] was utilized, which was chosen over the more established Drasdo and Fowler[23] conversion for greater consistency in retinal sphericity with Curcio and Allen's data.[21] This conversion was also subsequently

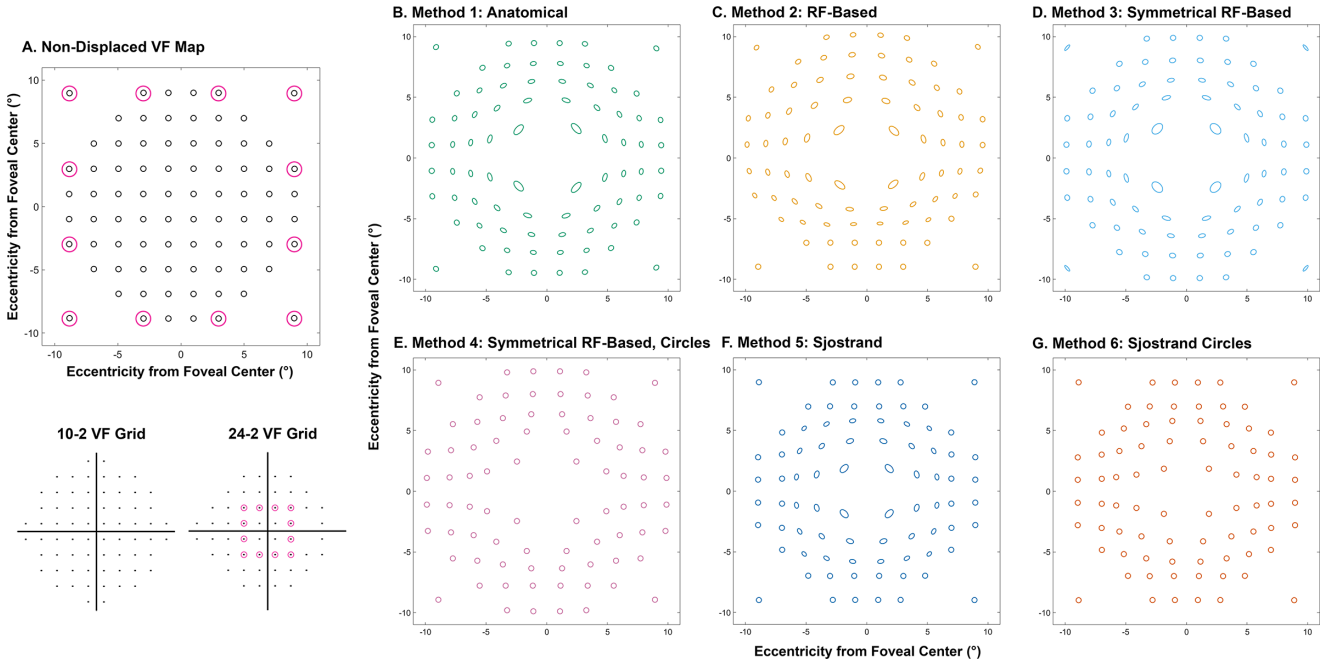

Figure 1. Maps depicting the different displacement models tested in this study. All plots are displayed in VF view and right eye format. (**A**) The VF map with the 10-2 and paracentral 24-2 test locations prior to displacement. (**B**) Method 1 (anatomic) used displacement based on Henle fiber length applied along the circumference of each VF test location. (**C**) Method 2 (RF based) used displacement computed from the difference between cumulative RGC RF and RGC body counts, applied along the circumference of each VF test location. (**D**) Method 3 (symmetrical RF based) used a similar principle to method 2, except with a single displacement curve utilized regardless of angular location. (**E**) Method 4 (symmetrical RF based, circles) used the same displacement curve as method 3, except with displacement of the VF test location center only. (**F**) Method 5 (Sjöstrand) applied displacement per the Sjöstrand model along the circumference of each VF location. (**G**) Method 6 (Sjöstrand, circles) used the Sjöstrand model with displacement of the VF test location center only.

applied as required in calculations throughout the study.

Displacement Models and Comparison of Midget RGC to Cone Ratios

Displacement models were compared at retinal locations consistent with projected 10-2 test grid locations using a Goldmann III stimulus size, as per the Humphrey Field Analyzer (Carl Zeiss Meditec, Dublin, CA, USA). This paradigm was chosen as it is a common procedure for functional testing of the macula in clinical settings.[24] The 12 paracentral test points of the 24-2 grid, falling within the maximum displacement zone of 4.034 mm as per the Drasdo model, were also included. The polar coordinates of the stimulus center and 72 points along the stimulus circumference were calculated using a stimulus radius of 0.215°, for subsequent input to the displacement models.

This study applied four implementations of the Drasdo model that were coded using MATLAB version R2019a (MathWorks, Natick, MA, USA; Fig. 1). These implementations were based on variations of the Drasdo model applied across different studies of the structure–function relationship.[11,13,14,16,17]

- Method 1 (anatomic): total displacement based on Henle fiber length along the VF stimulus circumference with differences in nasal and temporal meridians, as per Figure 2 in Drasdo et al.[12]
- Method 2 (receptive field [RF] based): displacement based on differences in location for equivalent cumulative RGC RF counts ($C_{RGC\text{-}RF}$) and histologic C_{RGC} per Curcio and Allen,[21] calculated along the VF stimulus circumference. The derivation of this meridian-specific model is described in the appendix of Drasdo et al.,[12] with analogous methods applied in subsequent studies.[11,16] Details of the calculations involved are presented in Supplementary Methods 1.
- Method 3 (symmetrical RF based): as per method 2 but with total displacement averaged across all principal meridians rather than applying meridian-specific differences, as per Figure 6 in Drasdo et al.[12]
- Method 4 (symmetrical RF based, circles): as per method 3 but with displacement of the VF stimulus center only. While methods 1 to 3 produce elliptical areas, method 4 maintains circular areas per projected Goldmann III VF stimuli.

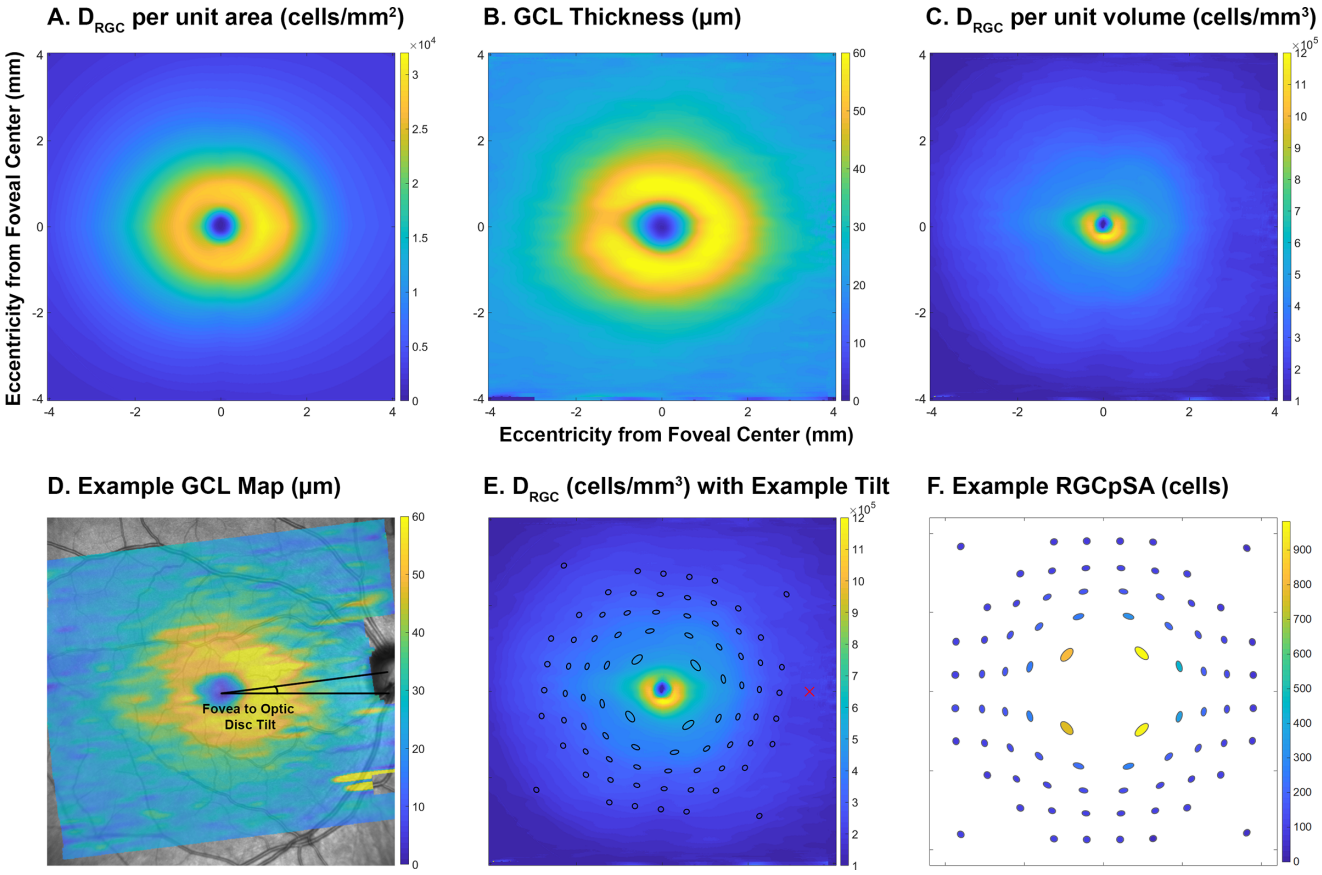

Figure 2. Generation of RGC volumetric data for individual RGCpSA calculation. (**A**) Map of RGC density (D_{RGC}) in cells per square millimeter, interpolated from principal meridian data from Curcio and Allen.[21] (**B**) GCL thickness map in micrometers, averaged across data from the modeling cohort. (**C**) D_{RGC} in cells per cubed millimeter, calculated from A and B. (**D**) An individual participant's GCL thickness map, with the foveal center and fovea to optic disc tilt annotated. (**E**) The displaced VF map per method 1 (Fig. 1B) superimposed on C, rotated according to fovea to optic disc tilt; D_{RGC} values were averaged over these areas for this fovea to optic disc tilt. The *red cross* indicates the optic disc center. (**F**) RGCpSA calculated from D and E.

The Sjöstrand model of RGC displacement relative to underlying cone eccentricity is described by the following equation[18]:

$$\text{RGC Eccentricity} = 1.29 \times (\text{Cone Eccentricity} + 0.046)^{0.67}$$

where both RGC and cone eccentricity are in millimeters. The mRGC:C ratios produced using this model were also implemented as below:

- Method 5 (Sjöstrand): with Sjöstrand displacement applied at the VF stimulus circumference.
- Method 6 (Sjöstrand circles): with Sjöstrand displacement applied at the VF stimulus center only, similar to method 4.

As the Sjöstrand model is only described up to 2 mm from the foveal center, locations beyond 2 mm eccentricity from the foveal center were not displaced.

As methods 1 and 2 require linear interpolation of displacement between the principal meridians, displacement curves were computed at 0.01 radian intervals. The angle components of the VF stimulus coordinates were subsequently rounded to the nearest 0.01 radians, and the corresponding displacement curve was applied to compute the displaced retinal eccentricity for each location using Akima spline interpolation. Methods 3 and 4 use a single displacement curve, and as such, the displaced retinal eccentricities were computed for the stimulus circumference points and centers with this curve regardless of direction from the foveal center.

The displaced VF stimuli were fitted with ellipse functions using a least squares fitting method for methods 1 to 3 and 5, as well as circular functions for methods 4 and 6, with MATLAB (Fig. 1 and Supplementary Figs. S1–S4), to minimize reduction of resolution at the displaced stimulus circumference with variable scaling. These were applied to the C_{mRGC} map to extract the number of mRGCs at each displaced VF location. Similarly, the nondisplaced VF

Table 1. Demographic Characteristics of the Included Cohort and Histologic Cohorts From Previously Reported Data[21,22]

	Current Cohort		Histologic Cohorts	
Characteristic	Modeling Cohort	Test Cohort	Curcio and Allen[21]	Curcio et al.[22]
Number of eyes	66	77	6	8
Age, mean ± SD (range), y	33.4 ± 4.0 (27.1–39.7)	32.8 ± 3.6 (27.0–39.8)	34.0 ± 3.6 (27.0–37.0)	34.8 ± 4.7 (27.0–44.0)
Spherical equivalent, mean ± SD, D	−1.40 ± 1.52	−1.32 ± 1.77	NA	NA
Fovea to optic disc tilt, mean ± SD, deg	6.57 ± 3.26	6.64 ± 3.31	NA	NA
Sex, M:F	36:30	32:45	3:3	3:5
Eye included, OD:OS	29:37	39:38	3:3	3:5

For the histologic data set, both eyes were included for some subjects. D, diopters; F, female; M, male; NA, not available; OD, right eye; OS, left eye; SD, standard deviation.

map was applied to extract the number of cones at each VF stimulus location. At corresponding VF locations, mRGC:C ratios were calculated by dividing C_{mRGC} by the number of cones, and these ratios were plotted against cone eccentricity using GraphPad Prism Version 8.4.3 (GraphPad Software, La Jolla, CA, USA). As Watson[19] derived eccentricity-dependent mRGC:C curves for each principal meridian using the same histologic data set, the averaged mRGC:C curve was used as the "ground-truth" model; this model was chosen over other mRGC:C ratios described in previous studies[18,20] due to its detailed description of eccentricity-based and meridional changes, requiring less interpolation between data points. Error for each displacement model was determined by calculating the difference between the mRGC:C ratio calculated over each VF location and that at the same eccentricity per the Watson model.[19] This enabled the calculation of the sum of squares of the residuals (SSR) and the root mean square error (RMSE), derived from the following equations:

$$\mathrm{SSR} = \sum_{1}^{n} (\mathrm{mRGC} : \mathrm{C}_{\mathrm{Watson}} - \mathrm{mRGC} : \mathrm{C})^2$$

$$\mathrm{RMSE} = \sqrt{\frac{\mathrm{SSR}}{n-1}}$$

where n denotes the total number of VF locations included for each method. As a point of comparison, mRGC:C ratios reported by Masri et al.,[20] using a different histologic data set consisting of six healthy human subjects, were plotted with the derived ratios.

To obtain estimates of variance around the SSR and RMSE values, the residuals were resampled using a previously described nonparametric bootstrap algorithm.[25] The data set was resampled 200 times, where 80 residual data points were reextracted and SSR and RMSE were calculated per sample. The mean bootstrapped SSR and RMSE values were then compared across methods using one-way analysis of variance (ANOVA) with Tukey's multiple comparisons tests.

OCT Data and Cohort Characteristics

For comparison of C_{RGC} estimates to clinical data, 143 participants aged 27 to 40 years were retrospectively recruited to represent an age-similar cohort to histologic data (Table 1).[21,22] Written consent for data to be used in research was obtained from all participants, and the study adhered to the tenets of the Declaration of Helsinki. All participants had attended Centre for Eye Health (Sydney Australia) for comprehensive examination, including slit-lamp biomicroscopy examination, intraocular pressure measurement, dilated fundus examination, VF assessment with standard automated perimetry, and OCT imaging of the macula and optic disc.[13,26,27] Inclusion criteria included spherical equivalent refractive error between +6.00 and –6.00 diopters, astigmatism less than –3.00 diopters, and absence of optic nerve and macular pathology; where one eye met these criteria, this eye was included for analyses, while if both eyes were eligible, one eye was chosen at random. Data from 128 participants have been included in previous studies.[13,26]

The study cohort was randomly allocated to either the modeling cohort, whose data were used to generate the regression and D_{RGC} models as described later, or the test cohort, whose data were subsequently

tested with the generated models. This was performed to ensure model performance was not inflated. As axial length may affect GCL and GCIPL measurements, analyses on a subcohort of participants in whom axial length data were available are described in Supplementary Methods 2; Centre for Eye Health clinical protocols do not include routine axial length measurements, and hence this information was not available for all participants.

OCT data were obtained using the Spectralis SD-OCT (Heidelberg Engineering, Heidelberg, Germany) with the posterior pole volume scan preset, which acquires 61 B-scans across a total retinal area of 30° horizontally and 25° vertically centered on the foveal pit. Per Tong et al.,[26] automatic segmentation of the GCL and IPL outer boundaries was reviewed and manually corrected by a single observer (JT) as required within the inbuilt segmentation correction function in the instrument review software (Heidelberg Eye Explorer Version 1.10.4.0; Heidelberg Engineering), and these data were extracted in RAW format. Similarly, the angle between the fovea and optic disc centers, or the fovea to optic disc tilt, was manually reviewed and corrected when required, and the extensible markup language (XML) file corresponding to OCT data was extracted with this information.

For implementations of the Drasdo model where the mRGC:C ratios were most consistent with the model derived by Watson,[19] averaged GCL and GCIPL thicknesses were extracted over the displaced VF locations without rotation of the VF grids to most closely resemble retinal locations sampled during VF testing.[26,28] This was not performed for implementations inconsistent with previously described mRGC:C ratios, which were used as the anatomic ground-truth model in this study. For locations where accurate delineation of the GCL and IPL boundaries could not be performed, such as due to blood vessel shadowing or poor signal strength, these locations were excluded from further analyses. A minimum overall signal strength of 15 dB was required per B-scan. Repeatability of these protocols for GCL and GCIPL segmentation is described in Supplementary Methods 3.

Comparison of RGC Counts from GCIPL versus GCL

Generation of volumetric D_{RGC} in cells per cubed millimeter is required to enable estimation of C_{RGC} from OCT data as previously described.[9,10] However, the extraction locations of GCL data relative to the fovea to optic disc axis vary depending on fovea to optic disc tilt, and therefore the corresponding D_{RGC} would also vary between individuals. To enable fovea to optic disc tilt-specific calculations, GCL thickness maps from the modeling cohort were rotated around the foveal center such that the fovea to optic disc was 0° and resized to a scale of 0.005 mm per pixel, enabling generation of an averaged pixel-wise GCL map across this cohort (Fig. 2). A volumetric D_{RGC} map in cells per cubed millimeter was then calculated by dividing the histologic D_{RGC} map by the averaged GCL map, and average D_{RGC} was extracted by rotating the displaced VF grid by the fovea to optic disc tilt to correspond to extracted GCL locations. For both the modeling and test cohorts, the number of RGCs expected to be stimulated across VF stimulus areas (RGCpSA) could then be calculated as per Yoshioka et al.[10]:

$$\mathrm{RGCpSA} = D_{RGC}\ \left(\mathrm{cells/mm^3}\right) \times \mathrm{GCL}\ (\mathrm{mm}) \times \mathrm{Displaced\ VF\ Area}\ \left(\mathrm{mm^2}\right)$$

with the displaced VF area calculated from the ellipse parameters for the corresponding displacement model (Supplementary Figs. S1–S4).

The feasibility of using GCIPL thicknesses to calculate $C_{RGC,SA}$ was determined by comparing outcomes from GCL thicknesses predicted from the GCIPL to measured GCL thicknesses for greater consistency with previously described methods. Regression analyses between GCIPL and GCL thicknesses were generated for the modeling cohort using GraphPad Prism. Proportions of the GCIPL occupied by the GCL were also plotted as a function of eccentricity in the modeling cohort for comparison with previous reports.[29] Bland–Altman comparisons between $C_{RGC,SA}$ derived from GCL thicknesses predicted from the optimal regression model and those from measured GCL thicknesses were then performed for the relevant displacement models. Additionally, to determine whether differences in predicted and measured GCL thicknesses varied with increasing RGCpSA, linear regression models were fit through Bland–Altman data, and whether the slope significantly differed from 0 was determined using the sums-of-squares *F*-test.

Results

mRGC:C Ratio Comparisons Between Drasdo Implementations

mRGC:C ratios derived from different displacement models, applied to retinal locations corresponding to the 10-2 and paracentral 24-2 VF stimuli, are depicted in Figure 3, with deviations from the averaged

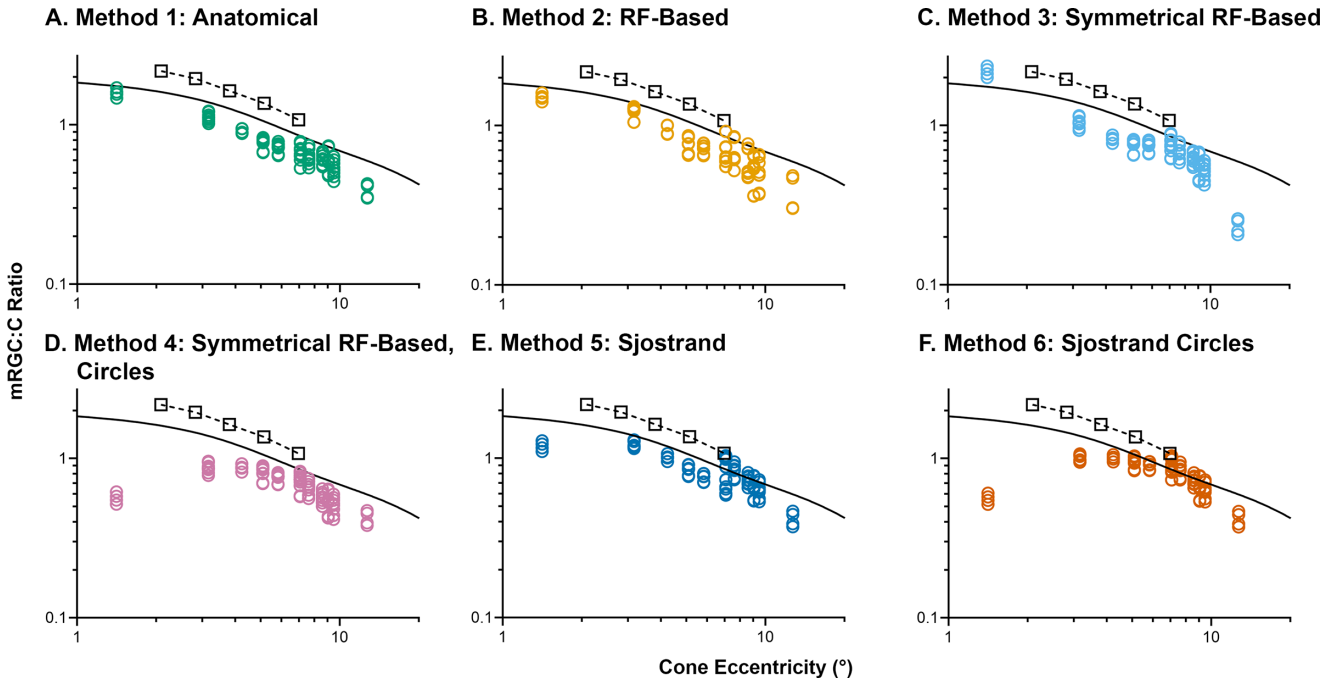

Figure 3. mRGC:C plotted as a function of cone eccentricity with the various tested implementations of the Drasdo and Sjöstrand displacement models. The averaged mRGC:C curve reported by Watson[19] (*black line*) and mRGC:C ratios reported by Masri et al.[20] (*black squares* and *dashed line*) are depicted as points of comparison. The x and y axes are in $\log_{10}$ units for consistency with Figure 14 in Watson.[19]

Table 2. SSR and RMSE, Calculated From Each Implementation of the Drasdo Model Relative to the Average mRGC:C Curve From Watson[19]

Characteristic	Method 1: Anatomic	Method 2: RF Based	Method 3: Symmetrical RF Based	Method 4: Symmetrical RF Based, Circles	Method 5: Sjöstrand	Method 6: Sjöstrand Circles
SSR						
Original	3.85	4.07	5.10	10.59	3.02	7.66
Bootstrapped	3.83 ± 0.30	4.07 ± 0.37	5.09 ± 0.60	10.32 ± 2.68	3.10 ± 0.61	7.68 ± 2.78
RMSE						
Original	0.22	0.23	0.25	0.37	0.20	0.31
Bootstrapped	0.22 ± 0.009	0.23 ± 0.010	0.25 ± 0.015	0.36 ± 0.046	0.20 ± 0.019	0.31 ± 0.057

These were calculated for the original data set and with bootstrapped data, where mean ± standard deviation values are reported.

Watson mRGC:C curve per the raw and bootstrapped data sets detailed in Table 2. Overall, method 5, using the Sjöstrand model applied to the circumference of projected VF stimuli, produced mRGC:C ratios most consistent with the Watson model, demonstrated by the smallest SSR and RMSE values and no eccentricity-based biases observed (Fig. 4). Of the Drasdo model implementations, methods 1 and 2, using meridian-specific displacement applied to the circumference of projected VF stimuli, were most consistent with the Watson model. In methods 1, 2, and 5, while central mRGC:C ratios all approached 2:1, as expected close to the foveal center, at peripheral locations, methods 1 and 2 appeared to slightly underestimate mRGC:C relative to method 5. Meanwhile, method 3, using a single displacement curve from the Drasdo model regardless of angular location, appeared to overestimate C_{mRGC} centrally and underestimate C_{mRGC} peripherally, with these errors reflected in the slightly larger SSR and RMSE values relative to methods 1, 2, and 5. Methods 4 and 6, in which only the stimulus center was displaced, appeared to underestimate C_{mRGC} and subsequently mRGC:C ratios at central locations, indicative of the relatively

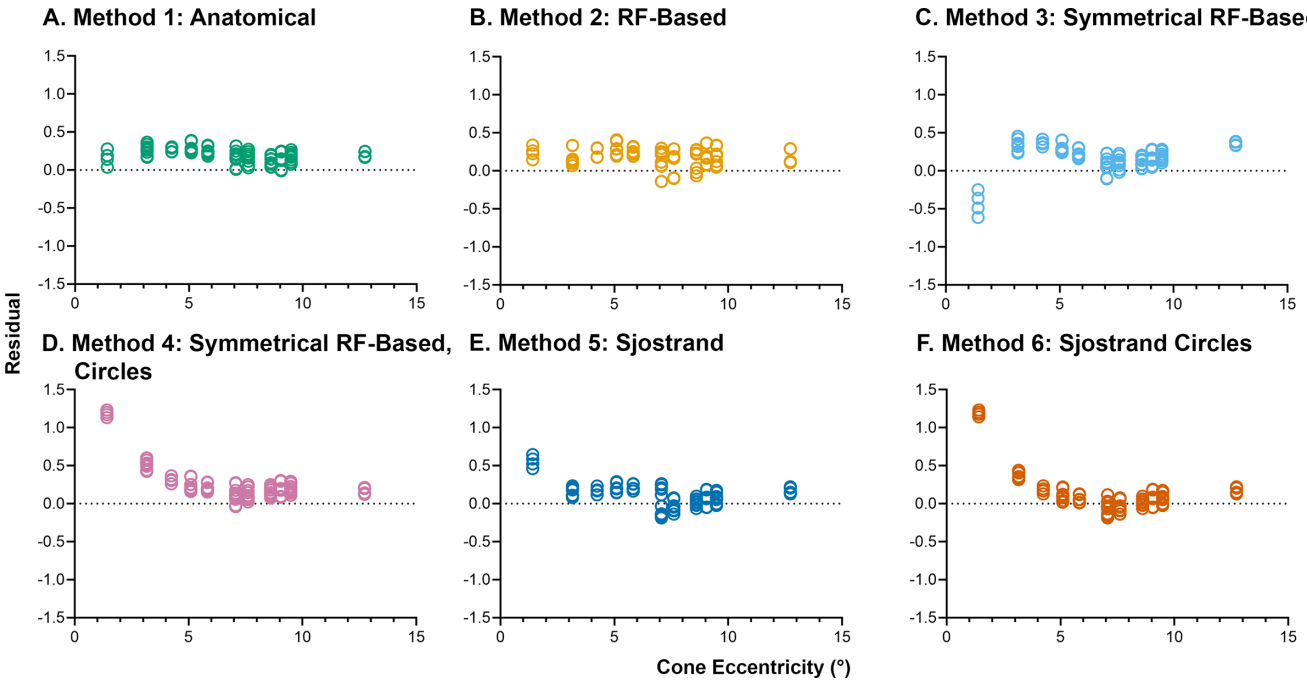

Figure 4. Error in calculated mRGC:C per implementations of the Drasdo and Sjöstrand models relative to the Watson model, plotted as a function of cone eccentricity. The y axis units are per Figure 3.

small area over which C_{mRGC} are calculated at these locations.

Bootstrapped analyses revealed no significant difference in bootstrapped SSR values between methods 1 and 2 but significant differences between all other comparisons ($P = 0.66$ between methods 1 and 2 and $P < 0.0001$ for all other comparisons), indicating significantly smaller SSR values with method 5 followed by methods 1 and 2. Similarly, RMSE values between methods 1 and 2 were not significantly different, with significant differences observed in all other comparisons ($P = 0.27$ between methods 1 and 2 and $P < 0.0001$ for all other comparisons). Overall, this indicates that method 5, based on the Sjöstrand model, was significantly more consistent with the Watson model than other displacement implementations tested, followed by methods 1 and 2 based on the Drasdo model.

mRGC:C ratios from Masri et al.[20] are also included in Figure 3. While the curve appeared to follow the trajectory of the Watson mRGC:C model, overall mRGC:C ratios were slightly greater than the Watson model and those derived in the present study. This is likely due to underlying differences in the histologic data, with greater C_{mRGC} and lower cone counts in Masri et al.[20] compared to the histologic data sets used in the Watson model and the current study.[19,21,22]

RGCpSA from Measured versus Predicted GCL

As methods 1, 2, and 5 produced mRGC:C ratios most consistent with ratios reported by Watson (Fig. 5 and Table 2),[19] only these methods were used for subsequent analyses investigating prediction of RGCpSA from OCT-derived GCIPL measurements. Regression models describing the relationship between GCIPL and GCL thicknesses were generated using data from the modeling cohort, with GCIPL and GCL thicknesses averaged over displaced VF areas. There was no significant difference in linear models with data averaged using method 1, 2, or 5 ($P = 0.95$). That is, a single linear model could sufficiently describe the relationship between GCIPL and GCL thickness, regardless of the areas over which measurements were obtained. The proportion of the GCIPL occupied by the GCL was relatively consistent from center to periphery in the modeling cohort (mean ± standard deviation, 55.19% ± 3.86%), with a greater proportion at relatively peripheral eccentricities than previously reported by Curcio et al.[29] However, there was a visible increase in data spread with increasing eccentricity in the included cohort.

This regression model enabled prediction of GCL thickness from the GCIPL, and predicted GCL values were subsequently used to estimate RGCpSA.

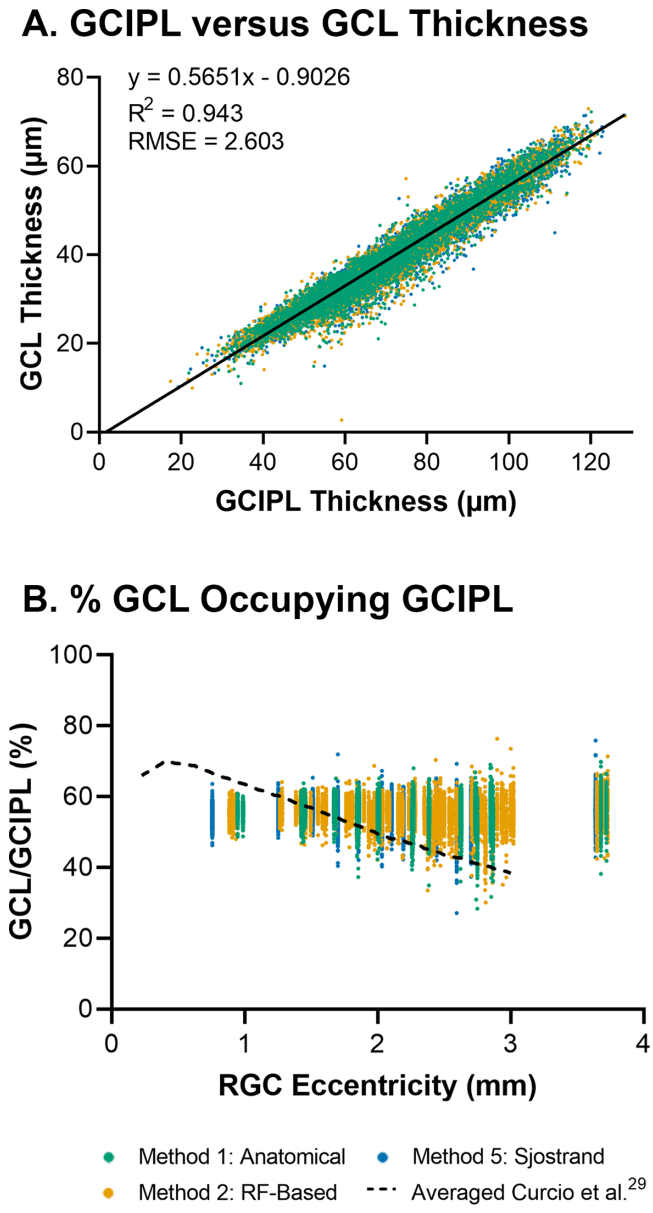

Figure 5. (**A**) Linear regression model describing the relationship between GCIPL thickness and GCL thickness in the modeling cohort. GCIPL and GCL thicknesses were averaged over displaced VF locations per methods 1, 2, and 5 (Fig. 1). Coefficient of determination (R^2) and RMSE for the shared linear regression model across all methods are also shown. (**B**) The percentage of the GCL occupying the GCIPL as a function of RGC eccentricity in the modeling cohort. Data averaged across temporal and nasal meridians from Curcio et al.[29] are included for reference.

Bland–Altman plots were then used to show agreement between measured and predicted GCL values in their estimation of RGCpSA. Within the modeling and test cohorts and using methods 1, 2, and 5, when expressed as a percentage of the averaged RGCpSA values, biases were close to 0%, and 95% limits of agreement (LoA) fell within 16.19%, indicating reasonable agreement between RGCpSA from predicted and measured GCL values (Fig. 6 and Table 3). Linear regression models through Bland–Altman data indicated no trend with increasing RGCpSA with the Sjöstrand model, but with the Drasdo model, there was a tendency toward underestimation at higher RGCpSAs overall (P = 0.002–0.02). However, the overall fits of the linear regression models were poor, demonstrated by low coefficients of determination (R^2 = 0.00004–0.001), and across the range of RGCpSA values, the maximum bias predicted from this linear regression model was 1.46%. This demonstrates that RGCpSA from predicted and measured GCL thicknesses appear equivalent irrespective of absolute RGCpSA values.

With Bland–Altman comparisons isolated to the central four locations, where the highest GCL thickness values and resultantly highest RGCpSA estimates are found, the 95% LoA narrowed to less than 13%, indicating greater agreement between RGCpSA from predicted and measured GCL values at these locations (Table 3). Meanwhile, when excluding the central four locations, 95% LoA remained similar to 16% across cohorts and methods, suggesting greater variability in predicted GCL thicknesses relative to the central four locations. However, at the 95th percentile of RGCpSA from measured GCL thicknesses, given reduced RGCpSA estimates at these relatively peripheral locations, this margin of error corresponds to a maximum difference in cell count of 60 RGCs across methods, indicating reasonable estimates of RGCpSA from GCIPL-derived GCL measurements.

Discussion

This study demonstrates that in order to obtain mRGC:C ratios consistent with histologic data, the Sjöstrand model or meridian-specific implementations of the Drasdo displacement model need to be applied at the circumference of VF stimulus locations. Additionally, GCL thicknesses can be predicted from GCIPL thicknesses as measured using OCT with reasonable accuracy, as shown by similar RGCpSAs from measured and predicted GCL thicknesses in the included healthy cohort. While numerous studies have used OCT-derived thickness measurements of inner retinal complexes such as the GCIPL as the structural measure in structure–function analyses,[14,30] thickness measurements are not direct indicators of the number of cellular units responding to stimuli. Therefore, by verifying the displacement models most consistent with histologic data and deriving estimates from clinically relevant OCT parameters, the described calculations aim to bridge the gap between structural measurements easily obtained using commercially available

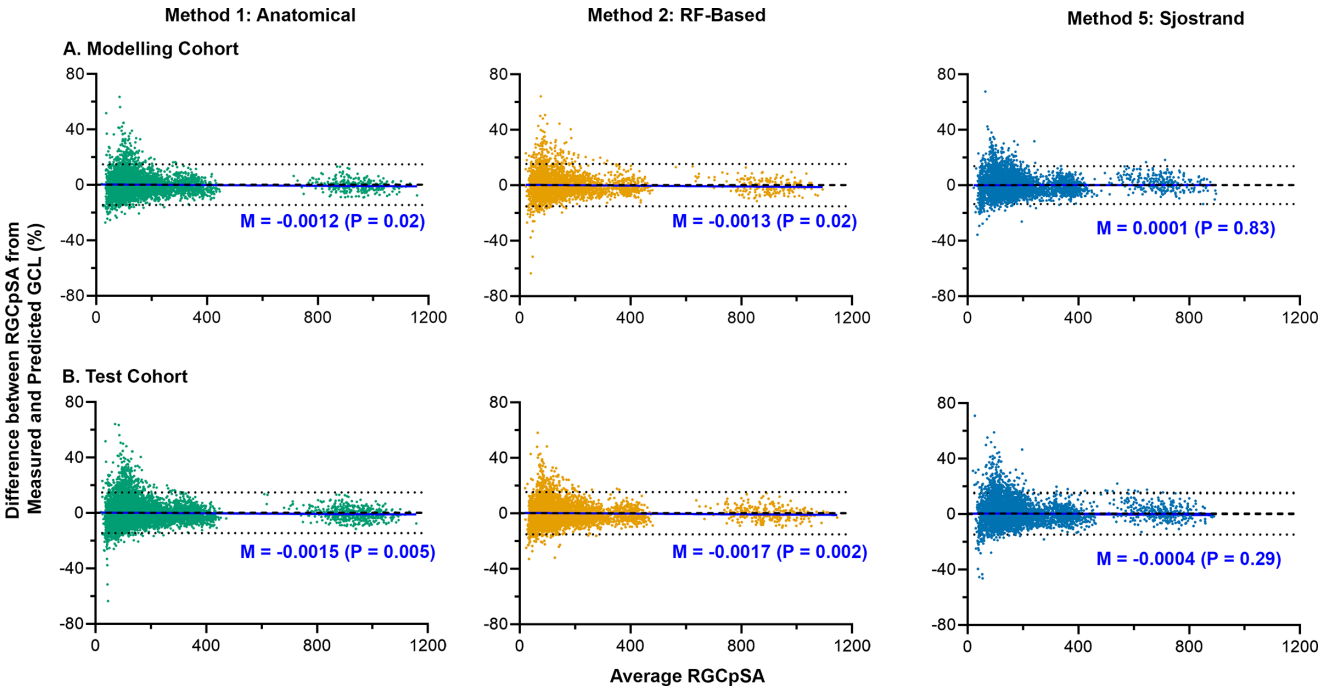

Figure 6. Bland–Altman comparisons between RGCpSA calculated from predicted versus measured GCL thicknesses for the modeling and test cohorts and for methods 1, 2, and 5, with predicted GCL thicknesses from GCIPL measurements as per Figure 4. *Black dashed* and *dotted lines* indicate the biases and 95% limits of agreement, respectively. The *dark blue solid lines* indicate the linear regression models through the data with corresponding slope values (M).

Table 3. Parameters for Bland–Altman Comparisons Within the Modeling and Test Cohort and Using Methods 1, 2, and 5, as per Figure 6

	Method 1: Anatomic			Method 2: RF Based			Method 5: Sjöstrand		
Characteristic	Bias	Upper LoA	Lower LoA	Bias	Upper LoA	Lower LoA	Bias	Upper LoA	Lower LoA
All data									
Modeling cohort	0.17	14.81	−14.46	0.17	15.43	−15.43	0.13	13.74	−13.47
Test cohort	0.39	16.07	−15.28	0.40	16.19	−15.40	0.40	15.49	−14.69
Central points only									
Modeling cohort	−0.20	8.03	−8.43	0.23	9.31	−8.86	2.03	12.22	−8.15
Test cohort	−0.28	9.10	−9.66	−0.07	9.85	−9.99	2.25	13.85	−9.36
All data excluding central points									
Modeling cohort	0.19	15.09	−14.70	0.17	15.68	−15.35	0.03	13.77	−13.70
Test cohort	0.43	16.37	−15.51	0.42	16.47	−15.62	0.30	15.53	−14.92

All parameters are expressed as percentages of the averaged RGCpSA value.

instrumentation and number of RGCs responding to VF stimuli, in line with established models of the structure–function relationship.[6–8]

Differences Between Displacement Model Implementations

The studied implementations of the Drasdo and Sjöstrand displacement models differ in several distinct ways additional to those described in the methods above, contributing to the differences in C_{RGC} and subsequently mRGC:C ratios. Specific to the Drasdo implementations, across the central four VF test locations where the magnitude of displacement increases most rapidly, the gradient of change is greater when using method 3, the symmetrical RF-based implementation, compared with methods 1 and 2, resulting in a larger displaced ellipse area and apparent

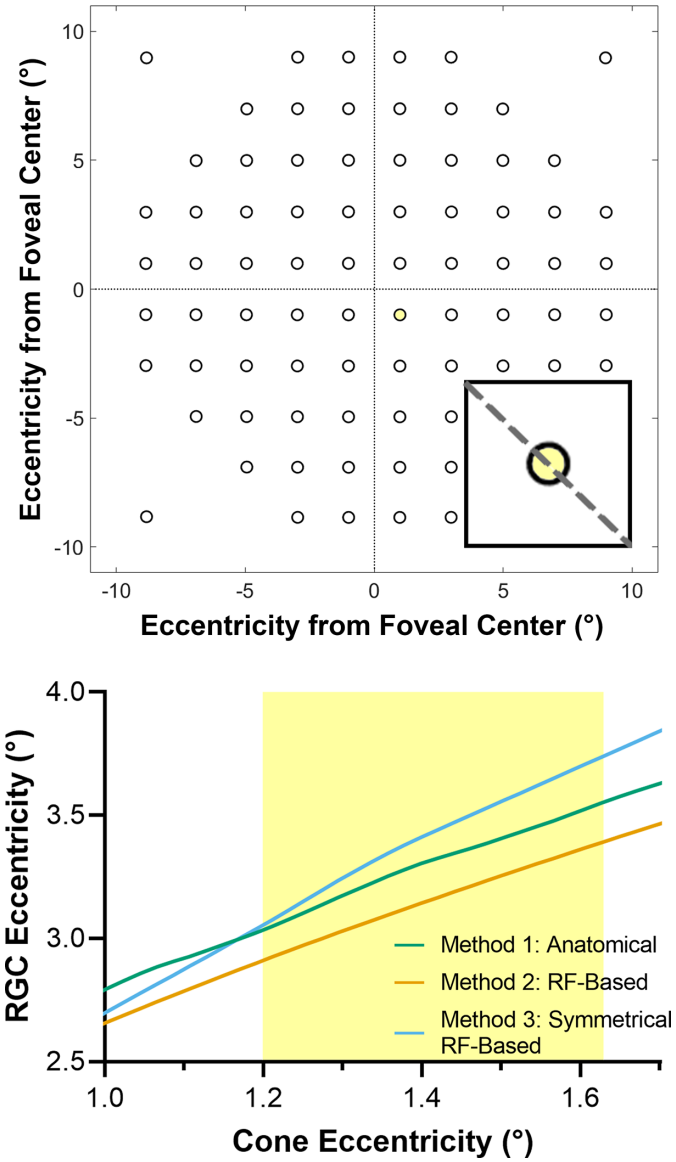

Figure 7. Differences in calculated displacement for different implementations of the Drasdo model along the –45 degree meridian (*gray dashed line*) for the inferonasal central VF test location (*yellow shading*). The gradient of the displacement curve across the VF test location for method 3 appears steeper than for methods 1 and 2, resulting in a larger ellipse area along this axis and contributing to greater C_{RGC} for method 3.

overestimation of C_{RGC} (Fig. 7). Similarly, for relatively peripheral locations, the progressive decrease in displacement with the Drasdo models produces relatively small ellipses compared to the Sjöstrand model, where no displacement was described beyond 2 mm, and resulting in apparent underestimation of C_{RGC} with the Drasdo model. However, this does not necessarily indicate that RGC displacement from corresponding cone pedicles does not occur at the perifovea, as previous studies have observed displacement up to 6 mm from the fovea.[20] Rather, this suggests a slower gradient of change in RGC displacement than suggested by Drasdo models. Interestingly, the maximum displacement as per Henle fiber measurements in the Drasdo model, 650 µm, is notably larger than in the Sjöstrand model and reported by other studies,[18,20] with shrinkage and differences in eye size reported as potential reasons for these differences. Nonetheless, the ability to derive meridian-specific displacements from the Drasdo model affords some advantage over these studies, and its widespread application is indicative of its relevance in studies of the structure–function relationship.

Application in Structure–Function Analyses

It is important to recognize that the similar mRGC:C ratios using methods 1, 2, and 5, based on measured Henle fiber length and cumulative RGC RF counts, respectively, may not translate to equivalent performance in structure–function analyses, which fell outside of the scope of the current study. In particular, method 5 assumes no meridional variations in RGC displacement, while method 1 assumes symmetry between superior and inferior fields; it is possible that meridional differences in RGC displacement will become more meaningful in comparison to functional data. Hirasawa et al.[17] reported poorer structure–function concordance with GCIPL thicknesses displaced according to methods 1 and 5 compared to no displacement outside of the central four VF test locations; given method 2 demonstrates a smaller magnitude of displacement in the inferior visual field relative to method 1, these results may indicate improved structure–function concordance with method 2. However, further investigations would be valuable to confirm which displacement model would be the most suitable.

GCL versus GCIPL Thickness From OCT

While several studies have compared structure–function relationships using various inner retinal complexes derived from OCT,[14,30,31] quantitative relationships between GCL and GCIPL thicknesses have not been modeled previously, which would be particularly valuable in settings where only the GCIPL is segmented by OCT software. It is perhaps unsurprising that the GCL can be predicted from the GCIPL with reasonable accuracy, given that the IPL corresponds histologically to the dendritic processes of RGCs among components, including bipolar cell terminals, astrocytic processes and dendrites, and Müller cell processes,[31,32] and thus proportional changes in the IPL with GCL may be expected. This

notion is supported by cluster analysis models demonstrating similar spatial patterns of aging in the GCL and IPL, with no significant differences in rates of change with age between these layers.[33] Interestingly, in both the modeling and test cohorts, the average proportion of the GCL occupying the GCIPL was 55.16% across the measured locations with no eccentricity-dependent variation, in contrast to previous reports of variations with increasing eccentricity.[29] In the cohort included in this study, considerably greater spread in the proportion of the GCL occupying the GCIPL was observed at more peripheral locations, likely due to the relatively poor discrimination of the GCL from the IPL using OCT, and this could contribute to the observed differences between studies. Despite greater variability in relative RGCpSA counts at these locations, given smaller absolute RGCpSA counts, this variability in predicted GCL thickness is unlikely to significantly affect estimated RGCpSA numbers.

Limitations and Conclusion

Several assumptions within the Drasdo and Sjöstrand displacement models may affect the findings of this study. As described earlier, Henle fiber measurements are described only for the horizontal meridian in the Drasdo model and for the vertical meridian in the Sjöstrand model, and quantitative histologic data and psychophysical data required for method 2 are reported for the principal meridians only; linear interpolation between meridians may not account for nonlinear variations in these data between meridians. Furthermore, the Watson model,[19] utilized as the anatomic "ground truth," uses data from 14 retinas only and therefore may not be representative of mRGC:C ratios across the wide spectrum of normal subjects, particularly when considering factors such as age, axial length, and refractive error. Further investigation comparing the relationship between RGC density and surrogate structural measures, such as adaptive optics OCT, would be warranted to confirm the necessity of compensating for these factors. Additionally, axial length data were available only for 30 participants (21% of the entire cohort), as routine axial length measurements are not conducted per Centre for Eye Health clinical protocols, so analyses with axial length could be conducted only on this subcohort (Supplementary Methods 2). While these analyses suggested that additional correction for axial length was not required, this is likely due to the strict refractive error inclusion criteria and does not necessarily indicate that corrections for axial length would not produce meaningful differences in RGC estimates, especially at axial length extremes. Further analyses with a more representative distribution of axial lengths would be valuable in identifying when axial length correction would be most beneficial. Finally, this study used measurements only from the Spectralis OCT; although previous studies have shown reasonable agreement between GCIPL measurements from Spectralis OCT and other devices,[31,34] confirmation of this study's findings with other instruments may be valuable to affirm suitability of GCL prediction from the GCIPL.

This study identified that meridian-specific implementations of the Drasdo model applied to the circumference of VF test locations are required to produce RGC numbers consistent with previous mRGC:C models. Moreover, a quantitative relationship between the GCL and GCIPL is described, which can be applied to estimate RGCpSA. By confirming the most appropriate implementations of the Drasdo displacement model and providing a means of obtaining RGC numbers from readily available OCT data, this study may help improve clinical implementations of the structure–function relationship.

Acknowledgments

The authors thank Barbara Zangerl for involvement in discussions on project direction and Paul Martin for guidance on preliminary calculations.

Supported by the National Health and Medical Research Council of Australia Ideas Grant (NHMRC 1186915) and an Australian Government Research Training Program Scholarship (JT). Additionally, Guide Dogs NSW/ACT provided a PhD scholarship (JT), salary support (JP and MK), and support clinical service delivery at the Centre for Eye Health. The funding bodies had no role in the conceptualization or writing of the paper.

Disclosure: **J. Tong**, None; **J. Phu**, None; **D. Alonso-Caneiro**, None; **S.K. Khuu**, None; **M. Kalloniatis**, None

References

1. Teller DY. Linking propositions. *Vision Res*. 1984;24(10):1233–1246.
2. Phu J, Kalloniatis M, Wang H, Khuu SK. Optimising the structure-function relationship at the locus of deficit in retinal disease. *Front Neurosci*. 2019;13:306.
3. Anderson RS. The psychophysics of glaucoma: improving the structure/function relationship. *Prog Retin Eye Res*. 2006;25(1):79–97.

4. Harwerth RS, Wheat JL, Fredette MJ, Anderson DR. Linking structure and function in glaucoma. *Prog Retin Eye Res*. 2010;29(4):249–271.
5. Malik R, Swanson WH, Garway-Heath DF. 'Structure-function relationship' in glaucoma: past thinking and current concepts. *Clin Exp Ophthalmol*. 2012;40(4):369–380.
6. Garway-Heath DF, Caprioli J, Fitzke FW, Hitchings RA. Scaling the hill of vision: the physiological relationship between light sensitivity and ganglion cell numbers. *Invest Ophthalmol Vis Sci*. 2000;41(7):1774–1782.
7. Swanson WH, Felius J, Pan F. Perimetric defects and ganglion cell damage: interpreting linear relations using a two-stage neural model. *Invest Ophthalmol Vis Sci*. 2004;45(2):466–472.
8. Harwerth RS, Carter-Dawson L, Smith EL, III, Crawford MLJ. Scaling the structure-function relationship for clinical perimetry. *Acta Ophthalmol Scand*. 2005;83:448–455.
9. Raza AS, Hood DC. Evaluation of the structure-function relationship in glaucoma using a novel method for estimating the number of retinal ganglion cells in the human retina. *Invest Ophthalmol Vis Sci*. 2015;56(9):5548–5556.
10. Yoshioka N, Zangerl B, Phu J, et al. Consistency of structure-function correlation between spatially scaled visual field stimuli and in vivo OCT ganglion cell counts. *Invest Ophthalmol Vis Sci*. 2018;59(5):1693–1703.
11. Montesano G, Ometto G, Hogg RE, Rossetti LM, Garway-Heath DF, Crabb DP. Revisiting the Drasdo model: implications for structure-function analysis of the macular region. *Transl Vis Sci Technol*. 2020;9(10):15.
12. Drasdo N, Millican CL, Katholi CR, Curcio CA. The length of Henle fibers in the human retina and a model of ganglion receptive field density in the visual field. *Vision Res*. 2007;47(22):2901–2911.
13. Tong J, Phu J, Khuu SK, et al. Development of a spatial model of age-related change in the macular ganglion cell layer to predict function from structural changes. *Am J Ophthalmol*. 2019;208:166–177.
14. Miraftabi A, Amini N, Morales E, et al. Macular SD-OCT outcome measures: comparison of local structure-function relationships and dynamic range. *Invest Ophthalmol Vis Sci*. 2016;57(11):4815–4823.
15. Raza AS, Cho J, De Moraes CG, et al. Retinal ganglion cell layer thickness and local visual field sensitivity in glaucoma. *Arch Ophthalmol*. 2011;129(12):1529–1536.
16. Turpin A, Chen S, Sepulveda JA, McKendrick AM. Customizing structure-function displacements in the macula for individual differences. *Invest Ophthalmol Vis Sci*. 2015;56(10):5984–5989.
17. Hirasawa K, Matsuura M, Fujino Y, et al. Comparing structure-function relationships based on Drasdo's and Sjostrand's retinal ganglion cell displacement models. *Invest Ophthalmol Vis Sci*. 2020;61(4):10.
18. Sjöstrand J, Popovic Z, Conradi N, Marshall J. Morphometric study of the displacement of retinal ganglion cells subserving cones within the human fovea. *Graefes Arch Clin Exp Ophthalmol*. 1999;237:1014–1023.
19. Watson AB. A formula for human retinal ganglion cell receptive field density as a function of visual field location. *J Vis*. 2014;14(7):15.
20. Masri RA, Grunert U, Martin PR. Analysis of parvocellular and magnocellular visual pathways in human retina. *J Neurosci*. 2020;40(42):8132–8148.
21. Curcio CA, Allen KA. Topography of ganglion cells in human retina *J Comp Neurol*. 1990;300(1):5–25.
22. Curcio CA, Sloan KR, Kalina RE, Hendrickson AE. Human photoreceptor topography. *J Comp Neurol*. 1990;292:497–523.
23. Drasdo N, Fowler CW. Non-linear projection of the retinal image in a wide-angle schematic eye. *Br J Ophthalmol*. 1974;58:709–714.
24. Phu J, Khuu SK, Yapp M, Assaad N, Hennessy MP, Kalloniatis M. The value of visual field testing in the era of advanced imaging: clinical and psychophysical perspectives. *Clin Exp Optom*. 2017;100(4):313–332.
25. Phu J, Bui BV, Kalloniatis M, Khuu SK. How many subjects are needed for a visual field normative database? A comparison of ground truth and bootstrapped statistics. *Transl Vis Sci Technol*. 2018;7(2):1–15.
26. Tong J, Alonso-Caneiro D, Kalloniatis M, Zangerl B. Custom extraction of macular ganglion cell-inner plexiform layer thickness more precisely colocalizes structural measurements with visual fields test grids. *Sci Rep*. 2020;10(1):18527.
27. Yoshioka N, Zangerl B, Nivison-Smith L, et al. Pattern recognition analysis of age-related retinal ganglion cell signatures in the human eye. *Invest Ophthalmol Vis Sci*. 2017;58(7):3086–3099.
28. Montesano G, Rossetti LM, Allegrini D, Romano MR, Garway-Heath DF, Crabb DP. Systematic and random mapping errors in structure-function analysis of the macula. *Transl Vis Sci Technol*. 2021;10(2):21.

29. Curcio CA, Messinger JD, Sloan KR, Mitra A, McGwin G, Spaide RF. Human chorioretinal layer thicknesses measured in macula-wide, high-resolution histologic sections. *Invest Ophthalmol Vis Sci*. 2011;52(7):3943–3954.
30. Mohammadzadeh V, Rabiolo A, Fu Q, et al. Longitudinal macular structure-function relationships in glaucoma. *Ophthalmology*. 2020;127(7):888–900.
31. Kim EK, Park HL, Park CK. Segmented inner plexiform layer thickness as a potential biomarker to evaluate open-angle glaucoma: dendritic degeneration of retinal ganglion cell. *PLoS One*. 2017;12(8):e0182404.
32. Xie W, Zhao M, Tsai SH, et al. Correlation of spectral domain optical coherence tomography with histology and electron microscopy in the porcine retina. *Exp Eye Res*. 2018;177:181–190.
33. Trinh M, Khou V, Zangerl B, Kalloniatis M, Nivison-Smith L. Modelling normal age-related changes in individual retinal layers using location-specific OCT analysis. *Sci Rep*. 2021;11(1):558.
34. Brandao LM, Ledolter AA, Schotzau A, Palmowski-Wolfe AM. Comparison of two different OCT systems: retina layer segmentation and impact on structure-function analysis in glaucoma. *J Ophthalmol*. 2016;2016:8307639.